An Advanced Model Predictive Current Control of Synchronous Reluctance Motors

Wagner Ruben Gaspar Benjamim

Dissertação para obtenção do Grau de Mestre em
Engenharia Eletrotécnica e de Computadores
(2º ciclo de estudos)

Orientador: Prof. Doutor António João Marques Cardoso
Co-orientador: Doutor Imed Jlassi

julho de 2021

Dedication

I would like to dedicate this body of work to my beloved mother, Victoria Francisco Gaspar Neto, for her constant encouragement and support, further instilling and cultivating a sense of responsibility within me since I was a young lad.

"*Aquele que acorda exigindo, madrugue cumprindo com os seus deveres*."

I would also like to dedicate this body of work to my beloved brother and sister, Victor Richard Gaspar Benjamim and Viviane Relíquia Gaspar Benjamim, respectively.

And, most importantly, I would like to dedicate this body of work to God for granting me strength and courage throughout my journey... a wild ride it was indeed...

"*Pursue what is meaningful (not what is expedient)*.".

Acknowledgments

To write is indistinguishable from thinking. The process of writing and compiling this body of work represents an inspiring yet challenging journey through the broadening of one's personal, academic, and professional horizons. Only by standing in the shoulder of giants, this journey was made possible. Gratitude is all I have for everyone that accompany me throughout this journey.

Firstly, I want to express my most profound and honest gratitude to my supervisor Professor António João Marques Cardoso, for believing in me by constantly providing guidance and support throughout these years and the work settings that made this Master thesis possible.

I want to express my sincere appreciation to my co-supervisor, Imed Jlassi, for the crucial help and technical support as well as the invaluable corrections and work ethic, further instilling in me lifelong skills through our time working together.

Furthermore, an appreciation is due to the members of CISE - Electromechatronic Systems Research Centre. Particularly to Fernando Bento for being helpful and considerate; furthermore, to Khaled Laadjal for being attentive and thoughtful and to André Barcelos for the friendship, mentoring and memories, although short-lived but with great intensity, nonetheless.

Lastly, to my family and friends, to whom I cherish and love, thank you for being there for me during all these years.

Wagner R. G. Benjamim

Resumo

Os motores síncronos de relutância (SynRMs) têm, nos últimos anos, atraído muita atenção devido às suas características construtivas, designadamente pela falta de materiais magnéticos caros, depreciando assim o custo em geral; e simultaneamente pelo aumento em robustez. Esses benefícios tornaram o SynRM num forte concorrente face a outros motores elétricos existentes no mercado. Da mesma forma, o modelo preditivo de controlo de corrente (MPCC) tornou-se recentemente numa poderosa estratégia de controlo avançado em acionamentos industriais, sendo, portanto, uma escolha adequada para acionamentos envolvendo SynRMs, garantindo elevado desempenho e eficiência de controlo. No entanto, a previsão da corrente no MPCC requer um grande número de vetores de tensão (VVs) sintetizáveis pelo conversor, sendo, portanto, exigente computacionalmente.

Consequentemente, o objetivo principal deste trabalho é o desenvolvimento e análise de um MPCC mais eficiente e avançado para SynRMs, reduzindo a carga computacional e, simultaneamente, demonstrando um bom desempenho de controlo em contraste com o MPCC clássico. Portanto, para atingir os níveis pretendidos de eficiência e desempenho de controlo em acionamentos com SynRMs, uma combinação de duas estratégias de controlo é desenvolvida, combinando o controlo de corrente de histerese (HCC) e MPCC, denominado neste trabalho HCC-MPCC. Além disso, as equações do modelo dinâmico do SynRM, compreendendo os efeitos de saturação magnética e as perdas de ferro, são apresentadas através de uma análise teórica e computacional detalhada do controlo do acionamento. Conclusivamente, o HCC-MPCC desenvolvido para acionamentos com SynRMs é analisado por meio de testes experimentais conjuntamente com o MPCC padrão, sendo os resultados obtidos detalhados de forma abrangente.

Palavras-chave

Modelo preditivo de controlo; Controlador de histerese; Esforço computacional; Motores síncronos de relutância

Abstract

Synchronous reluctance motors (SynRMs) have, in recent years, attracted much attention due to their high-efficiency output and nature of their construction denoted by the lack of expensive magnetic materials, thus cheapening the overall cost whilst increasing in robustness. These benefits have made the SynRM a strong contender against other established electric motors in the market. Similarly, model predictive current control (MPCC) has recently become a powerful advanced control technology in industrial drives, being, therefore, a suitable choice for SynRM drives granting overall high control performance and efficiency. However, current prediction in MPCC requires a high number of voltage vectors (VVs) synthesizable by the converter, being therefore computationally demanding.

Accordingly, the main goal of this work is the development and analysis of a more efficient and advanced MPCC for SynRMs whilst reducing the computational burden and delivering good control performance in contrast with the standard MPCC. Therefore, to achieve the intended levels of efficiency and control performance in SynRM drives, a combination of two control strategies is developed, which combines hysteresis current control (HCC) and MPCC, dubbed in this work HCC-MPCC. Furthermore, the SynRM dynamic model equations comprising the magnetic saturating effects and iron losses are presented through a detailed theoretical and computational analysis of the drive's control. Conclusively, the developed HCC-MPCC for SynRM drives is analyzed through thorough and rigorous experimental tests alongside the standard MPCC, whose obtained results are detailed comprehensively.

Keywords

Model predictive control; Hysteresis current control; Computational burden; Synchronous reluctance motors.

Table of Contents

List of Figures

List de Tables

List of Acronyms

IM	Induction Motor
PMSM	Permanent Magnet Synchronous Reluctance Motor
SynRM	Synchronous Reluctance Motor
FCS-MPC	Finite-Control-Set Model Predictive Control
MPC	Model Predictive Control
VVs	Voltage Vectors
MPCC	Model Predictive Current Control
2L-VSI	Two-Level Voltage Source Inverter
2L-BTB	Two-Level Back-To-Back Converter
DTC	Direct Torque Control
DPC	Direct Power Control
PMSG	Permanent Magnet Synchronous Generator
HCC	Hysteresis Current Control
PI	Proportional Integral
MTPA	Maximum Torque Per ampere
IGBT	Insulated Gate Bipolar Transistor
THD	Total Harmonic Distortion
IEEE	Institute of Electrical and Electronics Engineers
TWO	Total Waveform Oscillation
RMS	Root Mean Square

Chapter 1

Introduction

Electric machines can be described as an electromechanical energy converter, which can be called an electric motor or an electric generator if the conversion of energy is from electrical to mechanical or vice-versa. Due to the machines' versatility in energy conversion, they have found a wide range of applicability in several industry sectors as well as a widespread use in many areas including household appliances.

Given the widespread adaptability, use, and industry demand, electric motors have seen a considerable improvement in design since their inception to satisfy market needs such as overall performance, efficiency, and consumption. The induction motor (IM), for instance, is by far the most recognizable and used in the industry, accounting for roughly 40% of the electrical energy generated globally and consuming roughly 70% of the energy consumed in the European industry, making it the dominant type of load in this sector [1].

To deliver on its aforementioned popularity, the induction motor presents several advantages in its catalogue such as robustness, low cost, and the capacity to be connected directly to the grid. However, if the need for speed regulation is of primary concern, designs other than the induction motor become more attractive, and parameters like torque density (torque per volume), efficiency and control feasibility assume more importance [2].

To deal with the setbacks accompanying the induction motor, other types of electric motor designs have come into play in the last years. One of such designs is the permanent magnet synchronous reluctance motor (PMSM) that, compared to the IM, presents several advantages such as synchronous speed operation, higher power density, higher power factor, higher efficiency, and also including the capacity to be connected directly to the grid. Nevertheless, the PMSM has also some limitations, such as its difficulty of operating in the presence of high load inertia and the requirement of a high starting torque [1]. However, from all its possible limitations, the materials required in its construction, such as neodymium and dysprosium, are still costly and therefore non-viable for widespread acceptance.

On the other hand, another such design is the synchronous reluctance motor (SynRM), whose attractiveness in recent years has increased mainly due to its rugged characteristics, high efficiency, and the lack of expensive magnetic materials, further reducing its cost whilst increasing in robustness. Furthermore, even though the study of the SynRM dates to the 1920's [3], recent improvements in its rotor geometric configuration and drive technology made it a serious and strong contender against other established electric motors in the market, namely the IM and

PMSM, combing the best each one has to offer, which is simplicity and performance, respectively [4]-[7].

To achieve high control performance and efficiency from the SynRM drive, a suitable control technique is required. The finite-control-set model predictive control (FCS-MPC) has recently gained attention and notoriety [8]-[12]. It has distinguished itself from conventional control techniques, such as vector and direct control strategies, due to its ability to deal straightforwardly and intuitively with multi-objective control and integrate non-linearities and constraints into a pre-defined cost function while providing a fast dynamic response and superior performance.

Moreover, while it has been a matter of interest to the scientific community for more than three decades, only recent technical developments in digital signal processing have made it possible for emerging and more sophisticated control techniques such as model predictive control (MPC) to be applied to power electronics and drives [13][14]. Currently, MPC has come to incorporate a broad class of controllers depending on the application, operating principle, and other criteria [15]. Furthermore, different MPC control schemes can be found for a vast number of applications in power electronics [16].

However, MPC is not without its drawbacks. Mainly, the overreliance on the model of the system that requires prior information regarding the system and its intricacies, and the demand for high computational power compromise the initiative of MPC to become an industry-leading technology. Furthermore, concerning the latter issue, which is the main focus of this work, MPC demands a high computational burden due to all voltage vectors (VVs) combinations of the power converter used for prediction and evaluation [9]. As a result, as the complexity of the converter increases, so does the number of feasible VVs, and thus the computation effort. Consequently, long sampling times are required, resulting in large current ripples and a reduction in overall drive efficiency. Therefore, costly digital processors are needed to keep up with the computational demand, impacting the cost-effectiveness of MPC and subsequently inhibiting its broader acceptance in the industry.

Moreover, MPC solutions require sophisticated algorithms to achieve superior efficiency at the expense of computational effort. The literature survey presented in the subsequent chapters shows a substantial shortage of research into a practical and easy MPC scheme, i.e., model predictive current control (MPCC) that offers attractive characteristics such as simplicity, high control performance and low computational effort.

Therefore, in light of the aforementioned, the main objective of this work is the study, development, and analysis of computationally efficient MPCC for SynRM drives. The computational efficiency is achieved by reducing the number of VVs used to predict the current and evaluate the cost function, thereby decreasing the algorithmic execution time. To accomplish the reduction in VVs, a MPCC based on hysteresis comparators is proposed, developed, and implemented. Conclusively, for better analysis and detailed assessment of the computational

efficiency as well as the drive system performance, the proposed MPCC based on hysteresis comparators is contrasted against the classical MPCC.

1.1 Previous Studies in the Computational Efficiency of MPCC

As alluded to previously, because all VVs combinations of the power converter are required to predict the current and to evaluate the cost function, the MPC standard technique has an inherently high computing cost. For example, 8 VVs are used to predict and evaluate the cost function of a two-level voltage source inverter (2L-VSI). Furthermore, 16 VVs are used in a two-level back-to-back converter (2L-BTB). In addition, 32 and 64 VVs are needed for 5- and 6-leg converters, respectively. On the other hand, 27 and 125 VVs are required for MPC of 3L-VSI/matrix converter and 5L-VSI, respectively. The sampling time for MPC algorithms has been reported in the literature to be 50 μs for the 2L-VSI and 2L-BTB [10] and 100 μs for the 5-leg converter [11]. A sampling time of 65 μs is required for matrix converters [17]. In turn, sampling times of 52 μs and 93 μs are needed for the 3L-VSI and 5L-VSI, respectively [18].

Accordingly, the quantity of viable VVs increases with the complexity of the converter and hence the calculation effort. Moreover, high sampling times are further required, thus reducing the control efficiency. To deal with the issues previously mentioned, some predictive control strategies have recently been proposed. MPC is combined with a graphical approach to reduce the computation effort [19]. In [20], a control scheme based on a pre-defined voltage reference is implemented to predict only one VV in a 2L-VSI. In [21] and [22], deadbeat control is paired with MPC to select 3 out of the 8 predictions in 2L-VSI and 2L-BTB fed PMSM, respectively, resulting in less computational power being used. However, the graphical approach used in [19] is not intuitive and straightforward, and the deadbeat control algorithms used in [21] and [22] are complex and highly dependent on system parameters, being sensitive to parameter uncertainty.

Alternatively to complex MPC schemes, hysteresis-based control techniques are simple in both concept and implementation. For instance, in [23], direct torque control (DTC) and direct power control (DPC) were applied to permanent magnet synchronous generators (PMSG) drives, with results showing that the execution time is considerably lower than that of direct MPC. Consequently, given their straightforwardness, fast dynamic response and low parameter dependency, direct control techniques could present themselves as a solution, conferring significant advantages when paired with MPC techniques. In [24]-[26], a reduction of the candidate VVs and computation was achieved by reformulating new DTC switching tables and combining them with direct MPC. In [27], new DTC and DPC switching tables were combined with direct MPC of 2L-BTB fed PMSG, significantly reducing the number of candidates from 16 to 6 VVs and requiring less computation. DTC-based-MPC has also been proposed in [17] and [28] for matrix converter-fed PMSMs.

Furthermore, regarding the multilevel converters, a decrease in execution time was obtained by minimizing the number of VVs in 3L-VSI through the estimation of the position and deviation of the stator flux relative to its reference [29], an analysis of the voltage reference vector [30] or, a branch and bound approach [31]. For the 3L-BTB fed PMSG, again, the deadbeat based on system parameters is employed to reduce the candidate VVs, successfully decreasing the algorithm execution time [32].

Unfortunately, the solutions presented so far, although promising, still show some significant disadvantages, with most of the computationally efficient MPC being based on either a DTC switching table or deadbeat concept that, due to their need for system parameters, add further parameter dependency on the already heavily dependent predictive algorithms schemes, amplifying the adverse effects of a model-based predictive approach.

MPC solutions require sophisticated algorithms to achieve superior efficiency at the expense of computational effort. The literature survey shows a substantial shortage of research into a practical and easy MPC scheme that offers attractive characteristics such as simplicity, high control performance and low computational effort. On the other hand, hysteresis current control (HCC) bears a far more straightforward approach, both practically and conceptually, displaying a zero-parameter dependency on the system's model and less significant computational cost requirements.

Furthermore, a less computationally demanding MPCC based on HCC, which aims to obtain superior control performance, has not yet been reported in the literature. Accordingly, this body of work intends to solve the issues mentioned earlier, thus proposing a combination of HCC-MPCC for SynRM drives with enhanced control performance and robustness in the form of less parameter dependence in the HCC while being low in both complexity and computational burden. As a result, the number of required VVs is effectively reduced from 8 to 4 VVs; consequently, a low computational time is achieved, requiring less sampling time and enhancing the control performance. The proposed control algorithm is tested and validated by intensive experimental results.

1.2 Structure of the dissertation

The content of this body of work is structured into five chapters. Chapter 1 is restricted to a brief introduction to the subjects related to this dissertation to contextualize the presented work and elucidate its relevance. Furthermore, the main contributions and the structure of the dissertation are briefly described. Moreover, a revision of the state-of-the-art regarding the computation efficiency of the classical MPCC is also presented.

Chapter 2 starts with a brief introduction to the SynRM and its principle of operation, further highlighting its importance and contextualizing its use in this work. Moreover, an overview of its

inherent nonlinear intricacies is also presented, followed by a description of the SynRM drive and its mathematical model.

The theory of the classical model predictive current control is outlined as well as a computationally efficient control scheme for SynRM drives based on hysteresis controllers is presented and proposed, respectively, in Chapter 3. Furthermore, a detailed introduction to the control schemes involved is presented.

Chapter 4 begins with assessing the proposed control scheme's computational effort compared to the classical MPCC. Furthermore, the control performance of the control schemes involved is further detailed. Then, simulation and experimental tests are conducted with the results verifying the merits of the proposed method in relation to the classical strategy by using key evaluation parameters, such as computational burden and qualitative/quantitative analyses of the waveforms of the measured quantities. Moreover, the performance of the control strategies involved is analyzed under standard operating conditions.

In Chapter 5, the main conclusions of this dissertation are drawn, and some topics for future research in this field are pointed out.

Chapter 2

Mathematical Model of the SynRM

As the SynRM drive is an intrinsic part of the control techniques applied, a characterization of the machine's behavior through the development of an appropriate mathematical model with sufficient precision is essential for control performance.

Firstly, regarding its construction, the SynRM presents a very similar structure, build and configuration to other conventional electrical motors, namely in its frame, ventilation, bearings, stator, and windings, including its minor components. However, as the name suggests, the SynRM differs significantly from its counterparts, i.e., the IM and the PMSM, for its use of the reluctance principle, which directly influences its rotor design, giving rise to a unique configuration [33].

The SynRM rotor design presents a magnetic anisotropic axially laminated structure that generates a variable magnetic reluctance by presenting areas of low and high magnetic resistance referred to as the direct axis or d-axis and the quadrature axis or q-axis, respectively. As excitation currents are applied to the stator windings by a three-phase voltage system, a rotating magnetic field will be generated in the air gap; thus the rotor will aim to align its higher magnetic conductive axis, the d-axis, with the generated field in order to lower the magnetic reluctance in the magnetic circuit. Therefore, a magnetic toque arises from the proclivity of the rotor to align itself with the magnetic field at the minimum reluctance position [33].

As an electric machine made of ferromagnetic materials and non-ideal elements, the SynRM presents nonlinear characteristics inherently. Furthermore, such non-linearities propose a challenge to its control performance as it is affected by iron losses and magnetic saturation as well the cross-magnetization effects [34]-[37]. The saturation, as well as the cross-magnetization effects, can be observed as the magnetic flux interacts with the stator windings and the rotors ferromagnetic material promoting a variation of the stator inductance as well as the cross-saturation inductance in both direct (d-axis) and quadrature (q-axis) axes of the rotor. Moreover, it is worth noting that the saturation effect is different in both direct (d-axis) and quadrature (q-axis) axes due to the different nature of the magnetic flux paths [35] [38].

The dynamic model of the SynRM in the direct and quadrature (*dq*) reference frame can be obtained from the set of equations derived from the classical SynRM equivalent circuit as widely used in the literature [39]-[45]. The equations obtained using the *dq* rotor reference frame are much more simplistic in their composition than the *abc* stationary frame, thus easing the computational burden involved in the numerical computations in the control of the SynRM drive, further facilitating the implementation of the control system. The model of the machine used in this work considers that the saturation effect is negligible, and iron losses are dismissed. Thus,

the resulting equations become very simple with the aforementioned considerations, enabling the modeling of the machine behavior with reasonable precision.

Nonetheless, more complex dynamic models of the SynRM can also be defined to include the previously described nonlinear phenomena, namely the saturation effects and the iron losses, for an even more meticulous evaluation, as proposed throughout the literature. The impact of the cross-saturation effect in SynRM was extensively examined in [46]. A comparative study in synchronous machines with a highlight on the d-axis and q-axis saturation factors and their effect on the machine's transient response has been made in [47]. An analytical model, including saturation effects and cross magnetization, is introduced in [48]. An experimental study outlining the significance of the analytical representation of the saturation and cross magnetization effects in saturated synchronous reluctance machines is presented in [49]. Iron losses, together with saturation effects, have been included in a synchronous reluctance machine model using a vector control scheme in [35]. An inductance calculation method, as well as the iron loss and saturation effects in a synchronous reluctance motor (SynRM), is shown in [50].

However, given their complexity, the definition of these models can be relatively complicated, with the results demonstrating very little advantage in cost-effectiveness between the models mentioned above. Furthermore, given the necessity for more parameters, additional computational power is necessary.

2.1 Dynamic Model

As previously stated, given the complexity in the description and analysis involved in the mathematical modeling of the SynRM, the synchronously rotating reference frame fixed to the rotor is commonly used. In contrast to its counterpart, the *abc* stationary frame, the *dq*0 reference frame, as it is also known, allows for a significantly less complex set of equations that describe the SynRM due to the simplification that occurs by applying a change of variables, thus eliminating the time-varying aspect of the variables involved and the non-linearity characterized by the *abc* stationary frame, enabling for a simple and equivalent description of the model of the SynRM. Such change of the variable is commonly referred to as the Park's transformation, which enables the transformation of the state variables from an *abc* stationary frame to a *dq*0 rotating reference frame fixed on the rotor, through the transformation matrix defined as:

$$\begin{bmatrix} v_d \\ v_q \\ v_o \end{bmatrix} = \frac{2}{3} \begin{bmatrix} \cos(\omega_e) & \cos(\omega_e - \frac{2\pi}{3}) & \cos(\omega_e + \frac{2\pi}{3}) \\ -\sin(\omega_e) & -\sin(\omega_e - \frac{2\pi}{3}) & -\sin(\omega_e + \frac{2\pi}{3}) \\ \frac{1}{2} & \frac{1}{2} & \frac{1}{2} \end{bmatrix} \begin{bmatrix} v_a \\ v_b \\ v_c \end{bmatrix} \tag{2.1}$$

where ω_e is the rotor's electrical angular speed. On the other hand, the state variables in the a*bc* stationary frame can similarly be derived from the rotating *dq*0 rotating components through the inverse transformation matrix defined as:

$$\begin{bmatrix} v_a \\ v_b \\ v_c \end{bmatrix} = \frac{2}{3}\begin{bmatrix} \cos(\omega_{re}) & -\sin(\omega_{re}-\frac{2\pi}{3}) & 1 \\ \cos(\omega_{re}-\frac{2\pi}{3}) & -\sin(\omega_{re}-\frac{2\pi}{3}) & 1 \\ \cos(\omega_{re}+\frac{2\pi}{3}) & -\sin(\omega_{re}+\frac{2\pi}{3}) & 1 \end{bmatrix}\begin{bmatrix} v_d \\ v_q \\ v_o \end{bmatrix} \tag{2.2}$$

Figure 2.1 depicts the SynRM equivalent circuit in the dq reference frame. The resistor $R_c$inserted in parallel with the magnetizing branch in the dq axis models the iron losses [34]-[36].

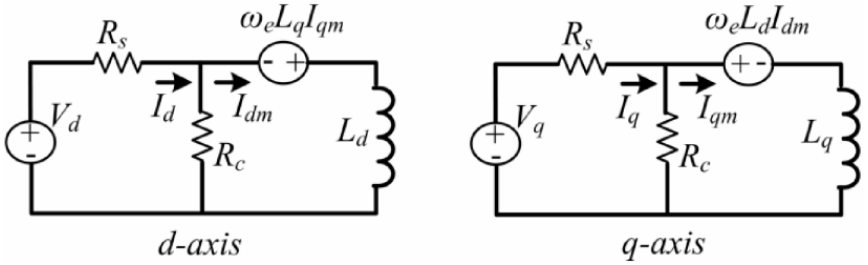

Figure 2.1: SynRM equivalent circuit in the dq axes reference frame: (a) d-axis; (b) q-axis. Adapted from [44].

Taking the above into consideration and given that the focus of this work is to reduce the number of VVs for MPC, thereby reducing the computational burden, the saturation effect of the SynRM is neglected for the sake of simplicity. Therefore, the stator voltage and current equations of the SynRM in a synchronous rotating frame can be expressed as follows:

$$\begin{cases} v_d = R_s i_d - \omega_e L_q i_{qm} + L_d \dfrac{di_{dm}}{dt} \\ v_q = R_s i_q + \omega_e L_d i_{dm} + L_q \dfrac{di_{qm}}{dt} \\ i_d = i_{dm} - \dfrac{1}{R_c}(\omega_e L_q i_{qm}) \\ i_q = i_{qm} - \dfrac{1}{R_c}(\omega_e L_d i_{dm}) \end{cases} \tag{2.3}$$

where L_d and L_q are the direct and quadrature inductances, v_d and v_q are the direct and quadrature axis terminal voltages, i_d and $i_q$are the direct and quadrature axis terminal currents, i_{dm} and i_{qm} are the direct and quadrature axis torque producing currents, R_s and R_c are the stator resistance and iron loss resistance per phase, and ω_e is the rotor's electrical angular speed. This is defined as a model without saturation. Since this model does not consider magnetic saturation, the inductances are assumed to be constant [41][51]. Given that the resistance R_c typically approaches very high values [44][52], and the motor used in this analysis is of high efficiency; hence the iron losses are dismissed [53]. Consequently, the torque producing currents i_{dm} and i_{qm} are made equal to the stator currents i_d and i_q, respectively. Therefore, given (2.3), the equivalent stator voltage equations can be expressed as:

$$\begin{cases} v_d = R_s i_d - \omega_e L_q i_q + L_d \dfrac{di_d}{dt} \\ v_q = R_s i_q + \omega_e L_d i_d + L_q \dfrac{di_q}{dt} \end{cases} \tag{2.4}$$

The state-space equations that allow for a complete SynRM dynamic model can be derived from (2.4), from which is given:

$$\begin{cases} \dfrac{di_d}{dt} = \dfrac{v_d - R_s i_d + \omega_e L_q i_q}{L_d} \\ \dfrac{di_q}{dt} = \dfrac{v_q - R_s i_q + \omega_e L_d i_d}{L_q} \end{cases} \tag{2.5}$$

The electromagnetic torque is given by:

$$T_e = \frac{3}{2} p (L_d - L_q) i_{dm} i_{qm} \tag{2.6}$$

On the other hand, the electromechanical torque, expressed by:

$$\begin{cases} T_e = J \dfrac{d\omega_m}{dt} + B_m \omega_m + T_L + T_K \\ \omega_m = \dfrac{\omega_e}{p} \end{cases} \tag{2.7}$$

where T_L is the load torque, J the inertia moment of the system rotating parts, ω_m is the motor's mechanical speed, B_m is the viscous friction coefficient, T_K the constant-coefficient load and p the number of pole pairs.

Chapter 3

Model Predictive Control

3.1 Classical Model Predictive Current Control

3.1.1 Model Predictive Current Control: An Overview

The classical MPCC that is a branch of MPC, can be described as an advanced control strategy that relies on the model of the system, including the VSI and the machine, to predict its future behavior within a prediction horizon based on an optimal user-defined criterion, thus ultimately generating the optimal behavior of the system. Specifically, MPCC predicts the behavior of variables to be controlled, i.e., the current, for each finite possible switching state generated by the VSI; thus, for the choice of the appropriate switching state to be applied, the selection criteria must be defined.

This criterion consists of a cost function that will be evaluated for the predicted values of the current, thus measuring the error between the reference and the predicted current. The current is calculated, i.e., predicted for each possible switching state of the VSI, then the state which minimizes the cost function is selected, thus ensuring that the error between the measured stator current and its reference value is small. Therefore, the general principle of the control algorithm has mainly three key constituents:

a. The dynamic mathematical model of the drive system.

b. A user-defined criterion, i.e., cost function, that ultimately generates the behavior of the system through a series of control action sequences over a prediction horizon *N*.

c. Optimization of the cost function. where only the optimal element of the generated control action sequences is applied, with the rest being disregarded. The control algorithm is then repeated in the next sampling period.

The general operating principle for MPC can be further seen in Figure 3.1, where, at sampling time *Ts* (in the ideal case), the measurements and the predicted system control actions are performed. The control actions are obtained by minimizing a cost function evaluating the best control action to take in the future. The optimal control action is then implemented, with measurement of the system variables and calculations being repeated in the next sampling time based on the system's state at said sampling time, thus generating new control actions with the prediction horizon being shifted forward. Nonetheless, for real-time discrete applications, introducing a longer step horizon is necessary due to the unfeasibility of performing the system's measurements and computing the control actions to be taken by the system simultaneously. Thus, a two-prediction horizon is often used [10].

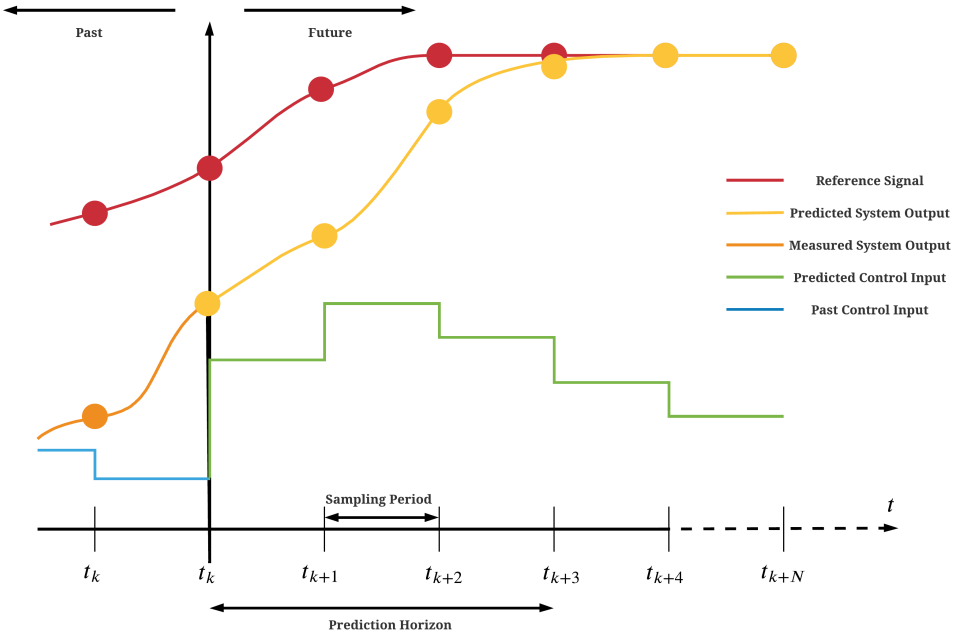

Figure 3.1: General concept of MPC.

In summary, MPCC deals well with complex dynamic systems subject to changes and allows for the inclusion of multiple constraints and non-linearities in the control system, resulting in a versatile control technique. The former is an intrinsic feature of industrial processes and real systems, posing a challenge to standard control techniques better-equipped control strategies to cope with less complex systems.

Moreover, a key difference from traditional optimal control, which uses a cost function for an overall assessment of the system performance over a prediction horizon, thus allowing for optimization of the control variables, i.e., the current. Furthermore, the predicted current output is based on previous information about the system and the predicted possible current values in the receding horizon, highlighting the model function of the system.

In particular, in MPCC, the optimal predicted values of the current are not obtained through the assessment of the error between the reference and the output feedback signals of the system, such as in the standard PID controller; the values of the current are obtained instead via cost function minimization serving as a performance function, i.e., the penalty for the future control actions, with only the optimal being selected and applied over a prediction horizon. In addition, MPCC is implemented as digital control.

Nonetheless, given the high customizability of the optimization problem, where various constraints and objectives can be added to the cost function, and the intended number of prediction horizons N, all for the sake of high control performance, the tradeoff is generally a high computation cost in MPCC. Several solutions to address this issue and its downsides have been introduced in Chapter 1. In the following section, another solution is further proposed.

3.1.2 Two-level-Voltage Source Inverter

In this work, the considered configuration of the drive system consists of a three-phase 2L-VSI linked to the SynRM. The VSI is characterized by six IGBT from T_1 to T_6 and their respective antiparallel diodes, where the control system outputs the optimal VV through a combination of the switching signals s_a, s_b and s_c. In addition, a closed-loop scheme with feedback sensors, where rotor location, stator currents and dc-link voltage V_{dc} are measured, is considered for high drive efficiency. The configuration of the SynRM drive system can be seen in Figure 3.2.

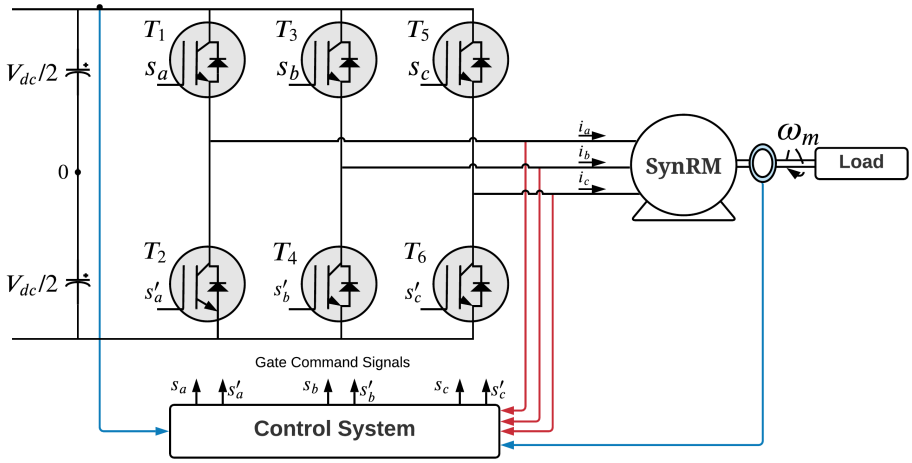

Figure 3.2: Configuration of the SynRM drive system with 2L-VSI.

A closer inspection of the VSI allow us to deduce the following mode of functioning for phase *a* as an example:

- *If* Switch T_1: ON; *then* Switch T_2: OFF; Thus, $S_a = 1, S'_a = 0$
- *If* Switch T_1: OFF; *then* Switch T_2: ON; Thus, $S_a = 0, S'_a = 1$

with the above being valid for phases *b* and *c*. Hence, the relationship between the phase (line-to-neutral) output voltage and switching states of the VSI is given by the following:

$$\begin{bmatrix} v_a \\ v_b \\ v_c \end{bmatrix} = \frac{V_{dc}}{3} \begin{bmatrix} 2 & -1 & -1 \\ -1 & 2 & -1 \\ -1 & -1 & 2 \end{bmatrix} \begin{bmatrix} S_a \\ S_b \\ S_c \end{bmatrix} \tag{3.1}$$

Given that for each of the three phases, there are two control actions defined by the ON-OFF activity of the switch, the voltage vector representation of the phase voltages corresponding to the eight different switching states/combinations that can be generated by the VSI can be calculated using the space vector definition where there are $2^3 = 8$ switching states, with the voltage space vector being defined as:

$$v_s = \frac{2}{3} V_{dc}(v_a + a v_b + a^2 v_c) \tag{3.2}$$

where the space rotation factor is given as $a = e^{j2\pi/3}$. The VSI output voltage in an equivalent in an $\alpha\beta$ stationary reference frame can be obtained by employing the following transform:

$$\begin{bmatrix} v_\alpha \\ v_\beta \end{bmatrix} = \frac{2}{3} \begin{bmatrix} 1 & -\frac{1}{2} & -\frac{1}{2} \\ 0 & \frac{\sqrt{3}}{2} & -\frac{\sqrt{3}}{2} \end{bmatrix} \begin{bmatrix} x_a \\ x_b \\ x_c \end{bmatrix} \tag{3.3}$$

Therefore, by employing (3.1) in (3.3), the VSI output voltage space vectors in its αβ are then given by:

$$\begin{cases} v_\alpha = \frac{2}{3} V_{dc} \left(S_a - \frac{S_b + S_c}{2} \right) \\ v_\beta = \frac{1}{\sqrt{3}} V_{dc}(S_b - S_c) \end{cases} \tag{3.4}$$

Evaluation of (3.4) for the different switching states yields the eight voltage space vector generated by the VSI as seen in Table 3.1, detailing the relationship between the output voltages and the eight conducing modes, i.e., switching states of the VSI is given in Table 3.1 where $V_j (j = 0, \dots, 7)$. Furthermore, it can be observed that the vectors generated are categorized into six active VVs (V_1 to V_6) and two "inactive" zero-VVs (V_0 and V_7). Moreover, the hexagon voltage vector can be seen in Figure 3.3, where the six active VVs define the axes of the VV hexagon and the zero-VVs at the origin, with the angle between two adjacent active vectors being 60 degrees. The relationship between the output voltages and the eight conducing modes, i.e., switching states of the VSI, is given in Table 3.1 where $S_j (j = 0, \dots, 7)$.

Table 3.1: VSI output voltage vectors

$V_j(s_a, s_b, s_c)$	v_a	v_b	v_c
$V_0(0,0,0)$	0	0	0
$V_1(1,0,0)$	$2/3\,V_{dc}$	$-1/3\,V_{dc}$	$-1/3\,V_{dc}$
$V_2(1,1,0)$	$1/3\,V_{dc}$	$1/3\,V_{dc}$	$-2/3\,V_{dc}$
$V_3(0,1,0)$	$-1/3\,V_{dc}$	$2/3\,V_{dc}$	$-1/3\,V_{dc}$
$V_4(0,1,1)$	$-2/3\,V_{dc}$	$1/3\,V_{dc}$	$1/3\,V_{dc}$
$V_5(0,0,1)$	$-1/3\,V_{dc}$	$-1/3\,V_{dc}$	$2/3\,V_{dc}$
$V_6(1,0,1)$	$1/3\,V_{dc}$	$-2/3\,V_{dc}$	$1/3\,V_{dc}$
$V_7(0,0,0)$	0	0	0

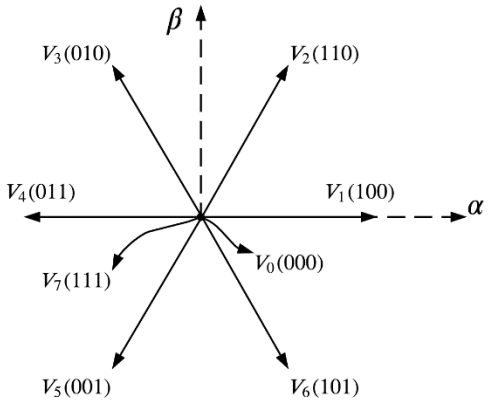

Figure 3.3: General VSI hexagon voltage space vectors.

It is worth noting that due to the existence of two zero-VV as seen in Table 3.1, several switching combinations can be generated. Nonetheless, it is common for real applications to choose one or the other to reduce the complexity in the implementation of MPC [54][55]. Hence in this work, V_0 is chosen as the zero-VV.

3.1.3 MPCC in SynRM drives

For the digital implementation of MPCC, a discretization method that approaches its continuous case is necessary. Given the small sampling time (T_s) used in this work, the forward Euler discretization method is deemed the most appropriate from the various discretization methods due to its simplicity, hence used in this work, thus being given by:

$$\frac{di(t)}{dt} = \frac{i[k+1] - i[k]}{T_s} \tag{3.5}$$

Initially, the equivalent stator voltage is reconstructed using the optimal VV as seen in (3.1) in the dq reference frame using (2.1). Therefore, considering the forward Euler discretization method (used throughout this work), the discrete-time version equations corresponding to (2.4) can be stated as:

$$\begin{cases} {v_d}^k = R_s {i_d}^k - \omega_e L_q {i_q}^k + \dfrac{L_d}{T_s}\left({i_d}^{k+1} - {i_d}^k\right) \\ {v_q}^k = R_s {i_q}^k - \omega_e L_d {i_d}^k + \dfrac{L_d}{T_s}\left({i_q}^{k+1} - {i_q}^k\right) \end{cases} \tag{3.6}$$

where T_s is the sampling interval, ${i_d}^k$ and ${i_q}^k$ are the direct and quadrature axis terminal measured currents at the $(k)th$ instant, and ${v_d}^k$ and ${v_q}^k$ are the direct and quadrature axis voltages obtained from the optimal VV applied to the VSI at the instant $(k)th$. Hence through (3.6), the predicted stator currents in the $(k+1)th$ sampling period are given by:

$$\begin{cases} {i_d}^{k+1} = \left(1 - \frac{R_s T_s}{L_d}\right) {i_d}^{k} + \omega_e T_s \frac{L_q}{L_d} {i_q}^{k} + \frac{T_s}{L_d} {v_d}^{k} \\ {i_q}^{k+1} = \left(1 - \frac{R_s T_s}{L_q}\right) {i_q}^{k} - \omega_e T_s \frac{L_d}{L_q} {i_d}^{k} + \frac{T_s}{L_q} {v_q}^{k} \end{cases} \tag{3.7}$$

Using the MPCC with delay compensation from [54] and according to (3.7), the predicted currents in the $(k+2)th$ sampling period can be written as:

$$\begin{cases} {i_d}^{k+2} = \left(1 - \frac{R_s T_s}{L_d}\right) {i_d}^{k+1} + \omega_e T_s \frac{L_q}{L_d} {i_q}^{k+1} + \frac{T_s}{L_d} {v_d}^{k+1} \\ {i_q}^{k+2} = \left(1 - \frac{R_s T_s}{L_q}\right) {i_q}^{k+1} - \omega_e T_s \frac{L_d}{L_q} {i_d}^{k+1} + \frac{T_s}{L_q} {v_q}^{k+1} \end{cases} \tag{3.8}$$

where ${v_d}^{k+1}$ and ${v_q}^{k+1}$are reconstructed from the 8 VVs of the hexagon voltage that the converter can synthesize. Then, the cost function is defined with an emphasis on the desired behavior of the SynRM. Therefore, considering that the implemented algorithm focuses on predictive currents, the cost function is then defined to evaluate the error between the predicted currents and their respective references. Hence, the cost function is given by:

$$g(k)|_{x_l} = \left[i_d^* - {i_d}^{k+2}\right]^2 + \left[i_q^* - {i_q}^{k+2}\right]^2; l = 0, \dots, 7 \tag{3.9}$$

In the SynRM control, a speed control loop with a proportional-integral (PI) controller generates the "command signal" from the error (difference) between the desired mechanical reference speed and the actual measured mechanical speed outputted by the machine with the goal of tracking the speed reference correctly, as seen in Figure 3.4. Given that the employed PI speed controller utilizes closed-loop control feedback, a speed sensor is also used to keep track of the machine's actual speed and obtain the location of the rotor. In addition, the performance of the PI speed controller is heavily dependent on its parametrization (controller gains), with the proportional component (*Kp*) being responsible for proportionally adjusting the command signal in relation to an existing error, i.e., speed offset; and with integral component (*Ki*) adjusting the control action to compensate for the steady-state error. The values assigned for the PI speed controller gains can be found in Appendix A. Hence the "command signal," i.e., the reference current i_q^* is generated by the PI speed controller, while i_d^* is derived from considering the MTPA strategy in [52], given by:

$$i_d^* = -0.0589 i_q^{*2} + 1.0515 i_q^* - 0.2374 \tag{3.10}$$

Therefore, by optimizing (3.9), the optimal VV can be determined as follows:

$$V_{VSI}(k) = \arg \min_{\{x_o, \dots, x_7\}} g(k)\,|_{x_l}; l = 0, \dots, 7 \tag{3.11}$$

where the optimal VV satisfying the criteria defined by (3.11) by which the chosen (minimal) value of the defined cost function g(k), will then be adopted to control the six insulated gate bipolar transistors' (IGBT') of the VSI in the $(k+2)th$ sampling period, according to Table 3.1.

Figure 3.4 shows a block diagram for the classical MPCC with a 2-step prediction horizon encapsulating the different elements previously detailed in this section, where a basic MPCC algorithm would be comprised of the following main steps:

1. Measurement of speed ω_e, stator currents ${i_{abc}}^k$ and reconstruction of voltages ${v_{dq}}^k$ and currents ${i_{dq}}^*$.
2. Apply the optimal VV $V_{VSI}(k)$ computed in the previous sampling time.
3. First step prediction of the currents ${i_{dq}}^{k+1}$ given the optimal VV $V_{VSI}(k)$ by (3.1)
4. Second step prediction of the currents ${i_{dq}}^{k+2}$ given the generated hexagon VVs by (3.8)
5. Evaluation of the predicted currents in the cost function and selecting the optimal VV through (3.9) and (3.11)

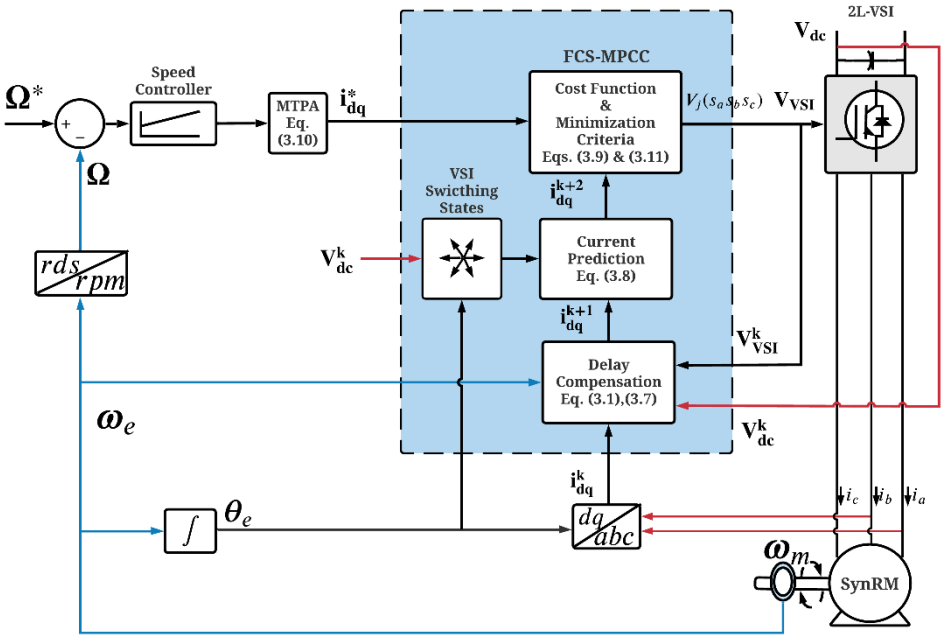

Figure 3.4: Block diagram of the Classical-MPCC.

MPCC offers some advantages, as previously indicated, for example, the easy addition of non-linearities and constraints. Nevertheless, the high calculations needed to solve the optimization problem, i.e., cost function minimization, limit its applications. Thus, in the following sections, this issue is addressed with the introduction of the proposed control scheme HCC-MPCC.

3.2 Proposed Model Predictive Current Control

The proposed control scheme HCC-MPCC intends to reduce the computational burden of the classical predictive scheme whilst maintaining an excellent control performance by combining the benefits of HCC with MPCC, thus also equipping the proposed control scheme with robustness and simplicity derived from the HCC and superior control performance, derived from MPCC. Ultimately, a lower execution time is achieved using 4 VVs for prediction and evaluation instead of all eight available VVs of the VSI whilst maintaining good control performance with minor current ripples.

Furthermore, given that the proposed control scheme combines two control schemes, namely, HCC and MPCC, the present chapter is divided into two sections. The working principle and the contribution of HCCs in the proposed control scheme are outlined in the first section of this chapter, with the following section integrating HCC into MPCC.

3.2.1 VVs Selection from HCC

HCCs, also known as bang-bang controllers, are among the most straightforward and intuitive control types. They work by directly controlling the motor phase currents whilst displaying its already mentioned benefits such as robustness, simplicity, excellent dynamic response limited merely by the switching speed and the load time constant, and independence of system parameters, making it attractive for this paper's intended purposes. The following expression summarizes the operation principle of HCCs:

$$S_x = \begin{cases} 1 \; if \; i_x^* > i_x + \dfrac{B_{hys}}{2} \\ 0 \; if \; i_x^* < i_x - \dfrac{B_{hys}}{2} \end{cases} x \in \{a, b, c\} \tag{3.12}$$

where S_x denotes the switching state of the upper semiconductor in the inverter arm of each phase, while the lower semiconductor takes the state complementary to the upper semiconductor, i_x and i_x^* are the actual current and the reference, respectively, where the subscript "x" denotes the phase, and B_{hys} denotes a defined hysteresis band.

The HCC control strategy is focused on the utilization of three hysteresis comparators to generate the converter gate signals, where each comparator has as an input the error between the measured current and its reference in the corresponding phase. The controllers then use the error in each phase to maintain their values within a defined hysteresis band B_{hys} , such that if the error crosses the upper band limit, the upper semiconductor is turned ON, and the lower semiconductor is turned OFF. Conversely, if the error crosses the lower band limit, the upper semiconductor is turned OFF, and the lower one is turned ON, thus maintaining the current within the hysteresis

band limits. Therefore, the hysteresis bandwidth sets the standard for the current tracking performance of the HCC.

Initially, the proportional-integral (PI) controller generates the torque-producing component (i_q), while the i_d component is obtained as a function of i_q according to the maximum torque per ampere (MTPA) detailed in the following section. Furthermore, the hysteresis bandwidth value is fixed for better control performance. Then, the reference VV is calculated by using three hysteresis comparators for each phase with the operation principle summarized by (3.12) and further detailed above in which each hysteresis comparator takes as an input the stator current, and its respective reference obtained from the transformation of the reference current components in the rotor reference frame to the *abc* reference frame, thus generating the initial reference VV. Subsequently, the near neighbor VVs to the initial reference VV are selected according to Table 3.2. For instance, if HCC computes the vector V_1 (green) as the reference VV, then the neighbor vectors V_0, V_2, and V_6 (red) are also selected. Figure 3.5 depicts the aforementioned scenario, where the reference and near neighbor VVs selection process are shown in green and red, respectively.

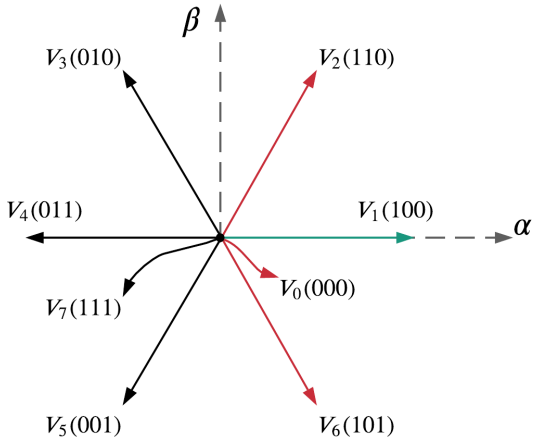

Figure 3.5: Hexagon VVs in the α-β frame and the corresponding switching states. HCC computed reference VV (green) and selected near neighbor VVs (red).

Similarly to the classical MPCC, it is also important to emphasize that the inverter allows for only eight switching states, resulting in six active-VVs and two identical zero-VVs at the origin of the coordinates, namely V_0 or V_7 . However, given the difficulty of differentiating between the two output voltages for the zero-VVs, choosing either switching states can significantly reduce the difficulty in implementation [55]. In terms of the scope of this work, only V_0 is defined as the zero-VV for the sake of simplicity and further reduction of the employed VV, to be used in conjunction with the active VVs, thus ensuring more ripple reduction [27]. Table 3.2 presents the relation of the near neighbor VVs ($N_{V_{HCC}}$) selection based on the HCC reference VVs (V_{HCC}) calculation where $V_{HCC}|_i (i = 0, \dots, 7)$. The selected 4 VVs will then be used in the proposed HCC-MPCC to predict the stator currents and determine the cost function. Subsequently, the optimal VV is chosen by minimizing the cost function presented in the next section.

Table 3.2: VVS Selection used in HCC-MPCC

$V_{HCC}\|_i$	$N_{V_{HCC}}\{x_0, x_1, x_2, x_3\}$
V_1	V_0,V_1,V_2,V_6
V_2	V_0,V_1,V_2,V_3
V_3	V_0,V_2,V_3,V_4
V_4	V_0,V_3,V_4,V_5
V_5	V_0,V_4,V_5,V_6
V_6	V_0,V_1,V_5,V_6
V_0 or V_7	V_0,V_0,V_0, V_0

3.2.2 HCC-MPC

Given that the proposed control scheme is built upon the classical MPCC framework, the equations corresponding to the predicted stator currents in the $(k+1)th$ and $(k+2)th$ sampling period are the same as equation (3.7) and (3.8), respectively. In the proposed HCC-MPCC, for (3.8), ${v_d}^{k+1}$ and ${v_q}^{k+1}$ are the direct and quadrature axis voltages computed from 4 VVs obtained from the HCC according to Table 3.2. However, in classic MPCC, ${v_d}^{k+1}$ and ${v_q}^{k+1}$are reconstructed from the 8 VVs of the hexagon voltage that the converter can synthesize, turning (3.8) into a computationally demanding task. Thus, the cost function is given by:

$$g(k)|_{x_l} = \left[i_d^* - {i_d}^{k+2}\right]^2 + \left[i_q^* - {i_q}^{k+2}\right]^2; l = 0, \dots, 3 \tag{3.13}$$

Furthermore, the reference current i_q^* is generated in the same framework of the classical MPCC (presented in the previous section and further valid for the proposed control scheme) considering the MTPA strategy in [52], given by (3.10).

Regarding Table 3.2, it can be further observed that each reference VV previously computed by the HCC V_{HCC} corresponds to a combination of 4 selected VVs $N_{V_{HCC}}$. Thus, yielding predicted current values through (3.8). Therefore, by optimizing (3.13), the optimal VV can be obtained by the following expression:

$$V_{VSI}(k) = \arg \min_{\{x_o, x_1, x_2, x_3\}} g(k)\,|_{x_l}; l = 0, \dots, 3 \tag{3.14}$$

where, in contrast to the classical MPCC, the optimal VV satisfying the criteria defined by (3.14) by which the chosen (minimal) value of the defined cost function g(k), is dependent on the 4-element VV; to be then employed to control the six insulated gate bipolar transistors' (IGBT') of the VSI in the $(k+2)th$ sampling period, according to Table 3.1 presented in the previous section.

In (3.8), (3.13) and (3.14), for the proposed HCC-MPCC control scheme, only four out of the eight available VVs of the VSI, previously calculated by the HCC, are used to perform the prediction of

the current and evaluation of the cost function within every sampling interval Ts; thus, computing the optimal VV, which is then applied to the converter.

However, it is essential to distinguish that, in the classical MPCC, all 8 VVs are used to predict the current and to evaluate the cost function. Similarly to the classical MPCC, the considered configuration of the drive system consists of a three-phase 2L-VSI linked to the SynRM, where the control system outputs the optimal VV through a combination of the switching signals s_a, s_b and s_c. Also, a closed-loop scheme with feedback sensors, where rotor location, stator currents and dc-link voltage are measured, is considered for high drive efficiency. Figure 3.6 shows the block diagram configuration for the proposed HCC-MPCC strategy in detail, encapsulating its different elements previously outlined in the relevant sections. The algorithm for the proposed control strategy is comprised of the following steps:

1. Measurement of speed ω_e, stator currents ${i_{abc}}^k$ and reconstruction of voltages ${v_{dq}}^k$ and currents ${i_{dq}}^*$.
2. Apply the optimal VV $V_{VSI}(k)$.
3. Computation of the initial reference VV V_{HCC} by the HCC through (3.12) and the neighbor VVs according to Table 3.2.
4. First step prediction of the currents ${i_{dq}}^{k+1}$ given the optimal VV $V_{VSI}(k)$ by using (3.7).
5. Second step prediction of the currents ${i_{dq}}^{k+2}$ given the selected VV in Table 3.2 by using (3.8).
6. Evaluation of the predicted currents in the cost function through (3.13) and selecting the optimal VV using (3.14).

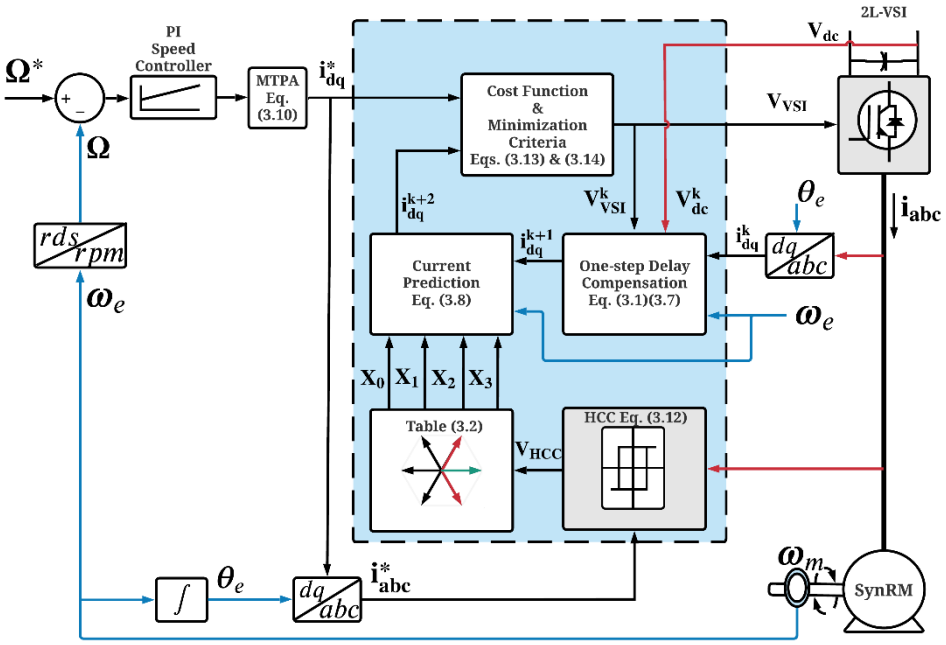

Figure 3.6: Block diagram of the HCC-MPCC.

Chapter 4

Simulation Results and Experimental Validation

4.1 Simulation Results

The Matlab/Simulink environment was used to theoretically evaluate and validate the considered control techniques for SynRM drives, i.e., the classical MPCC and the proposed HCC/MPCC presented in the previous chapter. Furthermore, the SynRM dynamic model described previously in Section 2.1 and other relevant parameters were taken into account in the computational modeling of the machine to bridge the gap between experimental equipment and the simulation environment. Table 4.1. contains the nameplate parameters of the used SynRM. In addition, Appendix A contains a complementary description of the SynRM parameters and other settings used in the simulation.

Table 4.1: Nameplate parameters of the used SynRM

Power	P	2.2 kW	Voltage	V	366 V
Speed	N	1500 rpm	Current	I	5.7 A
Nº of pole pairs	p	2	Torque	T_L	14 N.m
d axis inductance	L_d	0.24 H	q axis inductance	L_q	0.057 H

Figure 4.1 shows the simulation results under a speed progression and a load torque variation. Initially, the change in the speed reference from 1000 to 1500 rpm is given at t=1 s with an acceleration rate of 2500 rpm/s. The load torque is then increased its rated load torque value of 14 Nm at the instant t=1.5 s with the final speed reference set to 1500 rpm. The control performance of the classical MPCC and HCC-MPCC are presented in Figure 4.1(a) and Figure 4(b) respectively, with both control strategies evaluated at Ts=10 μs. Furthermore, both transient and steady-state operation modes are considered.

Careful examination of both classical and the proposed control strategies, whereas the classical MPCC makes use of more VVs than the proposed control strategy for the same sampling time of Ts=10 μs, indicates that the control performance of the SynRM drive is impacted by the number of VVs used for the prediction of the current and evaluation of the cost function, allowing for slight but considerable differences in the dynamic control response under variation in speed and step load torque as that categorizes the scenario shown in Figure 4.1.

Such impact is most distinguishably observed in Figure 4.1(a) from t=0.6s to t=1.2s, where for non-rated values of both speed and torque, the classical MPC showcases the worst control performance evidenced by a torque tracking capability that befalls in comparison to HCC-MPCC

in Figure 4.1. (b). In addition, although exhibiting a similar good speed tracking capability as the proposed control scheme, its torque tracking underperformance is mirrored in the *dq* axes currents yielding higher Total Waveform Oscillation (TWO) values further confirmed by observing the *dq* axes currents in low speeds settings in comparison to Figure 4.1. (b). On the other hand, with the adoption of the rated speed and torque values from t=1.2s onwards, the classical MPCC displays a slightly better control performance, evidenced by both *dq* axes and stator current waveforms presenting lower TWO values and a lower Total Harmonic Distortion (THD), respectively.

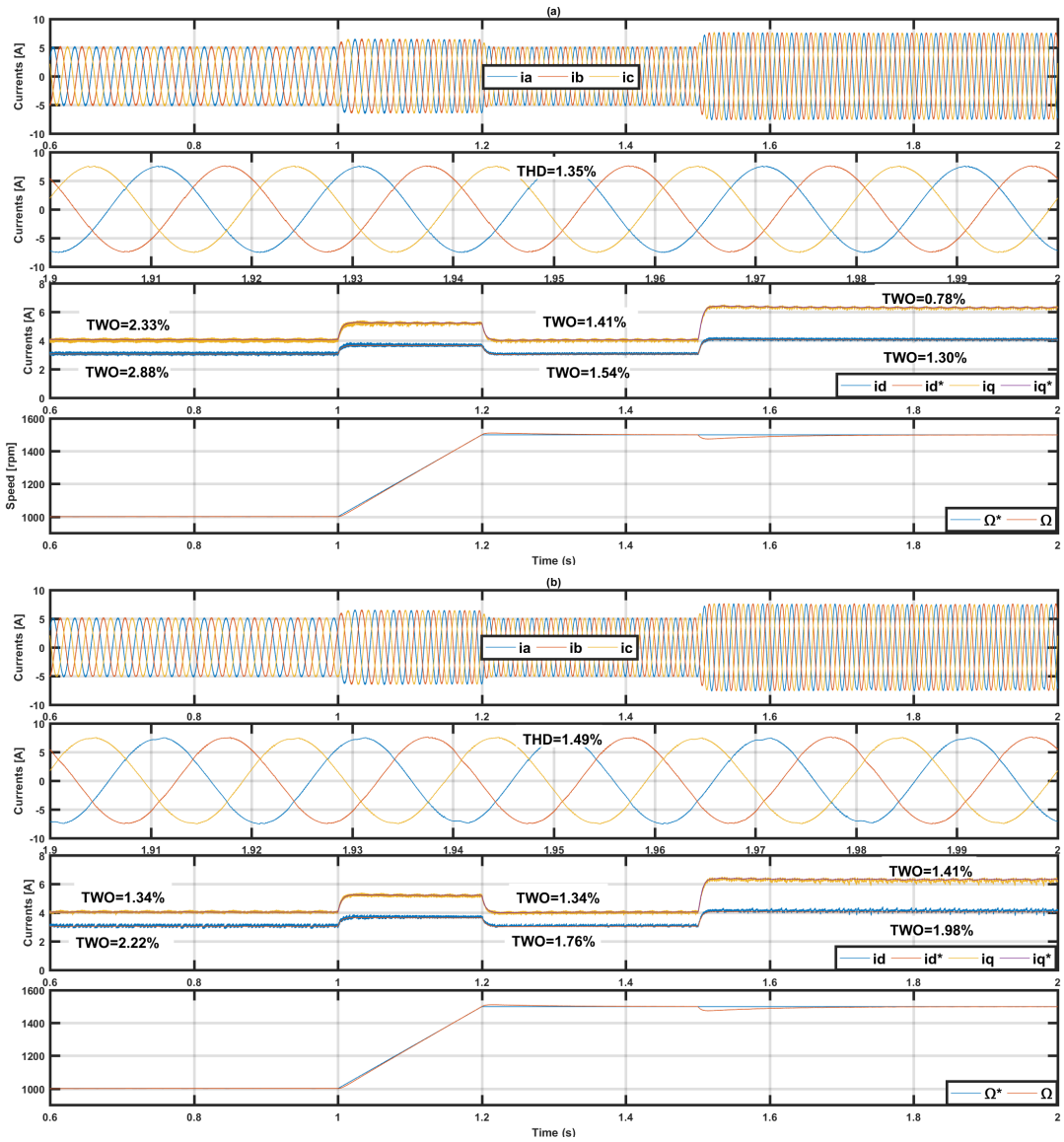

Figure 4.1: Simulation results: (a) MPCC (Ts = 10 μs), (b) HCC-MPCC (Ts = 10 μs), under speed and load torque variations.

Conclusively, it can be observed that both control strategies exhibit a similar rapid dynamic response for the considered operation conditions, showcasing good and precise speed tracking capability with no significant overshoot, leading to a well-tracked reference by the *dq* axes currents, displaying an excellent dynamic response under the speed progression, whilst handling well with quick torque variations. In addition, it can also be observed that the stator current

waveforms are effectively sinusoidal. Nonetheless, the differences and superiority of the proposed HCC-MPCC are further asserted and outlined in the following sections, with the introduction of the algorithmic execution time required by both control schemes in the experimental settings due to the use of a digital controller.

4.2 Experimental Validation

The feasibility of the considered control strategies for SynRM drives employed in this body of work was further experimentally evaluated in a laboratory setting. The experimental test rig comprises a 2.2 kW SynRM coupled to an AC electric machine used as a load, similar to the one used in the simulation scenarios detailed in the previous chapter. A Powerex POW-R-PAK VSI, a diode bridge rectifier and a dSPACE DS1103 digital controller are also part of the experimental configuration, as shown in Figure 4.2. The SynRM nameplate parameters used in the experimental setting are the same, detailed in Table 4.1.

The classical MPCC and the proposed HCC-MPCC algorithms are applied to the VSI. The same PI speed controller for closed-loop speed control is used for both control schemes. For the proposed HCC-MPCC, the hysteresis band is imposed to 0.2 A, approximately 3.5 % of the rated current, for better control performance.

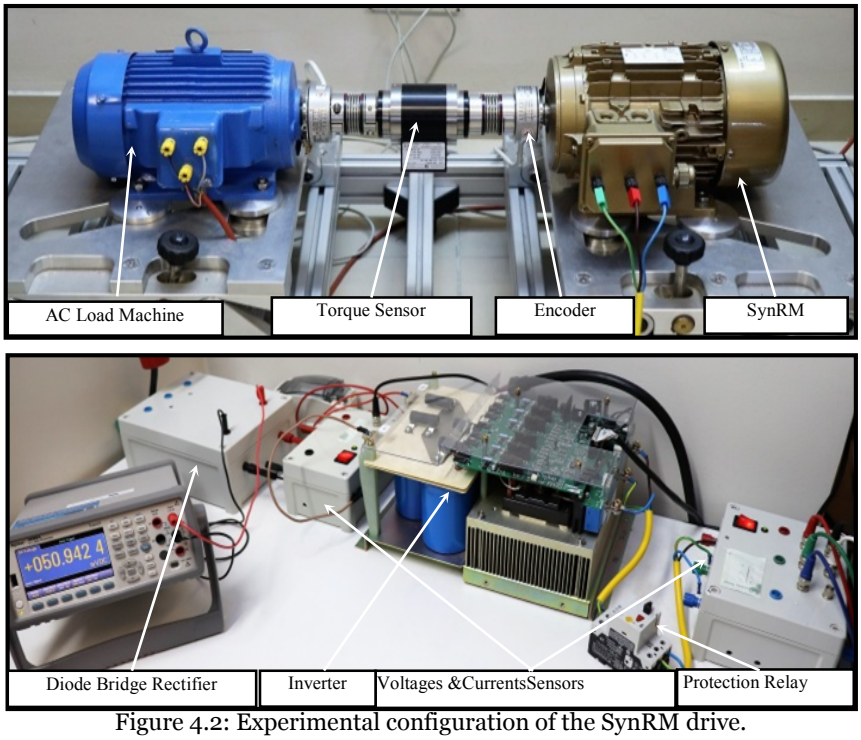

Figure 4.2: Experimental configuration of the SynRM drive.

4.2.1 Computational Effort

The classical MPCC and the proposed HCC-MPCC algorithms are separately implemented, under the Matlab/Simulink environment, into the dSPACE digital controller board. The computational prerequisites of a given algorithm are determined by the complexity and demands of the applied

programming language. One way to estimate such prerequisites is to calculate the computational effort placed on the controller in order to execute all the algorithmic calculations. Considering the procedure described in [56], Table 4.2 presents the average execution times taken by each algorithm in the dSPACE DS1103 controller and the real-time implementation details.

The computation effort of the proposed HCC-MPCC algorithm takes only 18.82 μs to complete the code, which is significantly lower than the classical MPCC execution time of 24.26 μs. Therefore, given that the sampling time Ts must be greater than the execution time and that the control variable ripples are heavily dependent on the Ts, the Ts for the classical MPCC cannot be considerably less than 35 μs due to the high algorithmic computation time. However, by using 4 VVs in the proposed HCC-MPCC, the Ts can be effectively reduced to 28 μs, thereby improving the overall performance of the control process.

Table 4.2: VVs Number and Execution Time of the HCC-MPCC and Classical MPCC.

Control algorithm	Number of VVs	Execution time (μs)	Sampling time (μs)
MPCC	8	24.26	35
HCC-MPCC	4	18.82	28

4.2.2 Control Performance

For an adequate assessment of the proposed algorithm's control efficiency and performance analysis, the total harmonic distortion (THD) expression is employed to quantify the distortion of the currents [27], further in compliance with the Institute of Electrical and Electronics Engineers (IEEE) guidelines specified in [57]. Similarly, the total waveform oscillation (TWO) factor is employed to quantify the ripple/oscillation content of said quantity, where a high ripple content is undesirable [27]. The THD can be expressed as:

$$THD = \sqrt{\frac{THD_A^2 + THD_B^2 + THD_C^2}{3}} \times 100\% \tag{5.1}$$

Furthermore, the TWO can be given by:

$$TWO = \frac{\sqrt{X_{eRMS}^2 - X_{eDC}^2}}{|X_{eDC}|} \times 100\% \tag{5.2}$$

where XeRMS and XeDC stand for the root mean square (RMS) values and average values of a given quantity, respectively. Extensive experimental tests were conducted to validate the proposed HCC-MPCC strategy, feasibility, and control performance. Furthermore, the classic MPCC is applied alongside the proposed algorithm for comparative purposes, however, with different sampling times. Both control schemes have been tuned in order to give the best possible performance, and they are tested under the same conditions. The performance evaluation

considers the analysis of the system's dynamic response to a set of operating conditions as well as the THD of the phase stator currents and the TWO values of the *dq* axes currents.

4.2.3 Experimental Results

Figure 4.3 shows a comparison between the classical MPCC at 35 μs (a), the proposed HCC-MPCC at 35 μs (b), and the proposed HCC-MPCC at 28 μs (c) under a step-torque load . The speed reference is set to 1000 rpm, whereas the load step-torque is applied at t = 0.5 s, ranging from 0 to 5 Nm. It can be observed that all control strategies exhibit a similar rapid dynamic response for the considered operation conditions, showcasing good and precise speed tracking capability, thus exhibiting their strength in withstanding rapid and load torque variations. Consequently, the *dq* axes currents present an expected behavior as they vary according to the demanded load torque displaying a good torque response. Moreover, it can also be observed that the stator current waveforms are effectively sinusoidal. Nonetheless, unlike the classical MPCC, the proposed HCC-MPCC does not test all the eight possible VVs of the VSI for evaluation and prediction, therefore the classical MPCC displays slightly better performance than the proposed HCC-MPCC for the same sampling time of Ts = 35 μs evidenced by the fact that for the same sampling time of Ts = 35 μs the classical MPCC (a) has an overall slightly better performance indicated by the lower TWO values and THD in dq axes currents and the stator current waveform respectively, in comparison with the HCC-MPCC (b), given the slightly higher TWO values and THD of the latter.

However, in contrast with the classical MPCC, as previously mentioned, the proposed HCC-MPCC reduces the VVs used for prediction and evaluation of the cost function, thus inherently requiring a shorter execution time, which translates itself to a shorter sampling time. Therefore, as indicated in Table 4.2, the sampling time of the proposed HCC-MPCC (c) is set to Ts = 28 μs; consequently, displaying superior control performance evidenced by the decrease in the overall TWO values in the *dq* axes currents, and subsequently a lower ripple content in the stator current waveforms in comparison with the previously mentioned control configurations, evidenced in the zoomed stator currents.

Furthermore, it is important to highlight that a shorter sampling time of Ts = 28 μs is not available for the classical MPCC, thus being set to Ts = 35 μs. In addition, it is also necessary to emphasize that given the MPCC's high parameter dependency on the SynRM model, slight deviations between the q axis current and its respective reference can be observed in Figure 4.3 for the employed control strategies. Moreover, the nonlinear nature of the operation conditions inherent to the experimental procedure and several other reasons are also contributing factors for the SynRM modeling accuracy.

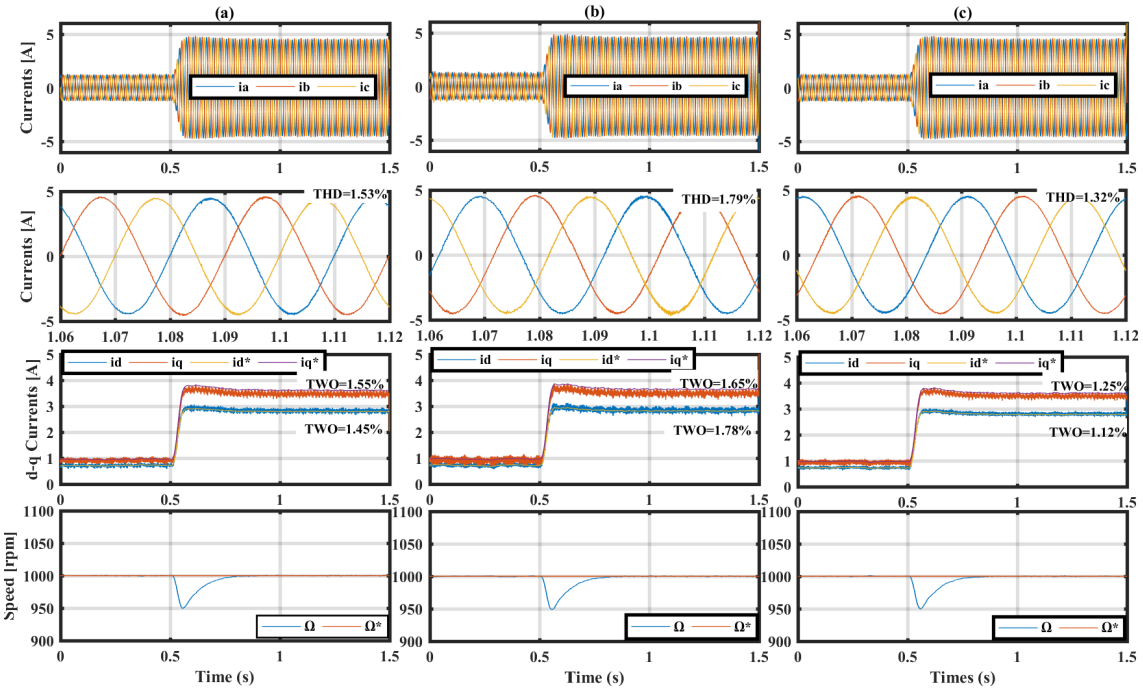

Figure 4.3: Experimental results: (a) MPCC (Ts = 35 µs), (b) HCC-MPCC (Ts = 35 µs) and (c) HCC-MPCC (Ts = 28 µs), under a step-torque load.

Figure 4.4 shows the control scheme performance under a speed progression from 500 to 1000 rpm, with a load torque of 2 Nm imposed to the SynRM. The change in the speed reference is given at t=0.5 s with an acceleration rate of 1000 rpm/s. It can be observed that for both MPCC and HCC-MPCC control strategies, the new speed reference value is tracked accurately and without any noticeable overshoot evidenced by the waveform smoothness under the employed speed progression. Similarly, the *dq* axes currents track their reference well, changing along with the speed progression displaying a great dynamic response in the transient state.

However, similarly to the previous operating condition, for the same sampling time of Ts = 35 µs, given its higher resolution, the classical MPCC (a) exhibits lower TWO values and ripple content in the *dq* axes currents and the stator current waveforms, respectively, in contrast with the proposed HCC-MPCC (b). Nonetheless, for the employed control strategy in Figure 4.4 (c) with a lower sampling time of Ts = 28 µs, it can be observed that the *dq* axes currents present low TWO values than the other control schemes configurations with a higher sampling time, consequently leading to sinusoidal stator currents with less harmonic distortion, showcasing the proposed HCC-MPCC superior control performance.

In summary, it deserves restating that, for the same sampling time of Ts= 35 µs, Figure 4.3 (b) and Figure 4.4 (b) showcase slightly higher TWO values and THD in *dq* axes currents and the stator current waveform, respectively, under both step-load torque and speed variations in comparison with the classical MPCC results in Figure 4.3 (a) and Figure 4.4 (a), that is, due to a lower resolution of the proposed control scheme at a sampling time of Ts=35 µs, with such occurrence lying in two main reasons.

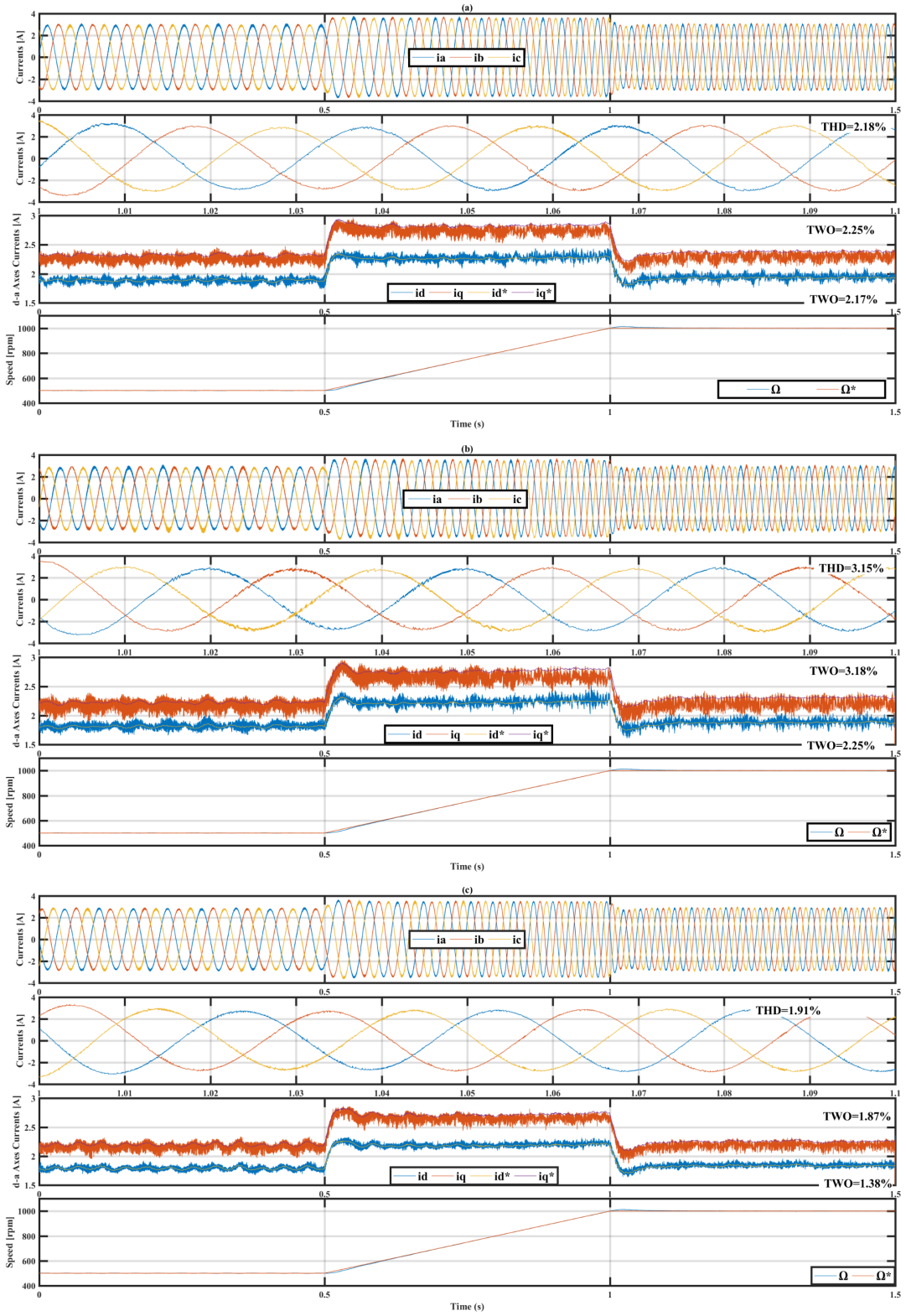

Figure 4.4: Experimental results of MPCC (Ts = 35μs), HCC-MPCC (Ts = 35 μs) and HCC-MPCC (Ts = 28 μs), under speed variations.

Firstly, the predicted vectors are selected based on the HCC reference VV, which is solely dependent on the HCC bandwidth. Secondly, not all feasible VVs are used for the prediction of the current and evaluation of the cost function. Nonetheless, it is essential to note that the computational running time for each algorithm's execution varies. Table 4.2 presents and

compares the average execution times of the algorithms. In comparison to conventional MPCC, the proposed HCC-MPCC eliminates the need for excessive calculations. As a result, the execution time is significantly reduced. In particular, the proposed HCC-MPCC dispenses with evaluating all feasible VV of the VSI, reducing the number of candidate VVs for prediction and evaluation in the cost function from 8 to 4VV. This ultimately reduces the algorithm's execution time.

Therefore, to reap the benefits of the related decrease in execution time, the sampling time can also be reduced. Thus, the sampling time can be set to 28 μs for the proposed HCC-MPCC, given that only 4 VV are evaluated, where a sampling time lower than 35 μs is not available for the classical MPCC. The implementation details in Table 4.2 reveal a 20% reduction in the excessive computational burden inherent to the classical MPCC. Further conceiving additional benefits to the proposed HCC-MPCC, thereby excelling, and showcasing the best control performance by exhibiting lower TWO values and THD in the *dq* axes currents and the stator current waveforms, respectively as shown in Figure 4.3 (c) and Figure 4.4 (c) compared to the classical strategy and further widening its applicability to cheap and less power-demanding microprocessors.

Chapter 5

Conclusions and Future Work

5.1 Conclusions

SynRM attractivity in recent years in relation to other electrical machines currently available and established in the market, given its sturdy characteristics, high efficiency yet simple in its structure, turn it into a solid contender, thus making the study and development of the SynRM drives into an exciting field of research. Therefore, given its popularity, an appropriate control technique is required to maximize the potential and widen the scope of applicability of the SynRM. The control technique of choice considered for this work is the predictive control technique, i.e., MPCC, due to its inherent advantages, such as fast control dynamics and overall good control performance. Nonetheless, the performance of the SynRM drive is highly affected by the MPCCs inherent computational burden.

Intending to address and provide a solution to MPCC's high computational cost, this body of work presents a computationally efficient HCC-MPCC control scheme of SynRM drives. The reduction in the computational cost has been achieved by a merger between the MPCC and the HCC; thus, defining only 4 VVs to predict the current and evaluate the cost function. Compared with the classical MPCC, the adoption of the proposed HCC-MPCC represents a reduction by 20% in the computational effort while simultaneously maintaining and exhibiting the best control performance, making it an attractive, cost-effective solution.

Moreover, the proposed HCC-MPCC scheme has further proven to improve on the inherent drawbacks of both HCC and MPCC, with the conducted experimental results also showing an overall reduction in the TWO values and harmonic distortion content and the ability to withstand parameters variability, yielding overall excellent results contrasted with HCC and MPCC alone.

5.2 Future Work

Several recommendations for future research can be made following up on the research and work developed throughout this dissertation, considering the relevance of predictive control techniques and SynRM drives:

- The development of a HCC-MPCC for SynRM drives with a variable/dynamic hysteresis band, thus ensuring an even better control performance, subsequently lowering the THD.
- The development of a HCC-MPCC for SynRM drives with a dynamic model accounting for iron losses and saturation effects differentiating between the apparent and the

incremental inductance, which is particularly important for the model-based techniques for current ripple reduction.

- Research and development of sensorless control techniques for SynRM drives.
- Research and development of fault-tolerant and fault diagnosis techniques for SynRM drives.

Bibliography

[1] J. Estima and A. J. M. Cardoso, "Efficiency analysis of synchronous reluctance motors," in *Proc. of the Int. Conf. on Engineering,* Nov 27, 2013, pp. 1-9.

[2] A. Boglietti and M. Pastorelli, "Induction and synchronous reluctance motors comparison," in *IECON Proceedings (Industrial Electronics Conference)*, 2008, pp. 2041–2044.

[3] J. K. Kostko, "Polyphase reaction synchronous motors," *J. Am. Inst. Electr. Eng.*, vol. 42, no. 11, pp. 1162–1168, Oct. 2013.

[4] S. M. Taghavi and P. Pillay, "A Sizing Methodology of the Synchronous Reluctance Motor for Traction Applications", IEEE Journal of Emerging and Selected Topics in Power Electronics,Vol. 2, No. 2, June 2014.

[5] T. Matsuo and T. A. Lipo, "Rotor Design Optimization of Synchronous Reluctance Machine," *IEEE Trans. Energy Convers.*, vol. 9, no. 2, pp. 359–365, 1994.

[6] R. Betz, R. Lagerquist, M. Jownovic, T. J. E. Miller and R. Middleton, "Control of Synchronous Reluctance Machines", IEEE Transactions on Industry Applications, Vol. 29, No. 6, pp. 1-6, 1993.

[7] A. Fratta and A. Vagati, "A Reluctance Motor Drive for High Dynamic Performance Applications," *IEEE Trans. Ind. Appl.*, vol. 28, no. 4, pp. 873–879, 1992.

[8] P. Cortes, M. P. Kazmierkowski, R. M. Kennel, D. E. Quevedo, and J. Rodriguez, "Predictive Control in Power Electronics and Drives," IEEE Trans. Ind. Electron., vol. 55, no. 12, pp. 4312–4324, 2008.

[9] S. Vazquez, J. Rodriguez, M. Rivera, L. G. Franquelo and M. Norambuena, “Model predictive control for power converters and drives: advances and trends”. IEEE Trans. Ind. Electron., Vol. 64, No. 2, pp. 935-947, 2017.

[10] S. Kouro, P. Cortes, R. Vargas, U. Ammann, and J. Rodriguez, "Model predictive control—a simple and powerful method to control power converters," IEEE Trans. Ind. Electron., vol. 56, no. 6, pp. 1826–1838, Jun. 2009.

[11] I. Jlassi and A. J. Marques Cardoso, "Open- circuit fault- tolerant operation of permanent magnet synchronous generator drives for wind turbine systems using a computationally efficient model predictive current control," IET Electr. Power Appl., Vol. 15, No. 7, pp. 837-846, June 2021.

[12] B. Gmati, I. Jlassi, S. Khojet El Khil, and A. J. Marques Cardoso, "Open-switch fault

diagnosis in voltage source inverters of PMSM drives using predictive current errors and fuzzy logic approach," IET Power Electron., Vol. 14, No. 6, pp. 1059–1072, May 2021.

[13] M. Morari and J. H. Lee, "Model predictive control: Past, present and future," in *Computers and Chemical Engineering*, 1999, vol. 23, no. 4–5, pp. 667–682.

[14] J. H. Lee, "Model predictive control: Review of the three decades of development," *International Journal of Control, Automation and Systems*, vol. 9, no. 3. pp. 415–424, Jun-2011.

[15] P. Cortés, M. P. Kazmierkowski, R. M. Kennel, D. E. Quevedo, and J. Rodriguez, "Predictive control in power electronics and drives," *IEEE Trans. Ind. Electron.*, vol. 55, no. 12, pp. 4312–4324, 2008.

[16] S. Vazquez *et al.*, "Model predictive control: A review of its applications in power electronics," *IEEE Industrial Electronics Magazine*, vol. 8, no. 1. Institute of Electrical and Electronics Engineers Inc., pp. 16–31, 2014.

[17] M. Siami, D. A. Khaburi, M. Rivera and J. Rodríguez, "A computationally efficient lookup table based FCS-MPC for PMSM drives fed by matrix converters," IEEE Trans. Ind. Electron., vol. 64, no. 10, pp. 7645-7654, Oct. 2017.

[18] V. Yaramasu, "Predictive control of multilevel converters for megawattwind energy conversion systems," Ph.D. dissertation, Dept. Electr. Comput. Eng., Ryerson Univ., Toronto, ON, Canada, 2014.

[19] J. Hu, J. Zhu, G. Lei, G. Platt and D. G. Dorrell, "Multi-objective model-predictive control for high-power converters," IEEE Trans. Energy Conversion, vol. 28, no. 3, pp. 652-663, Sept. 2013.

[20] Y. Zhang and W. Xie, "Low complexity model predictive control single vector-based approach," IEEE Trans. Power Electron., vol. 29, no. 10, pp. 5532–5541, Oct. 2014.

[21] W. Xie, W. X. Wang, F. Wang, W. Xu, R. M. Kennel, D. Gerling, and R. D. Lorenz, "Finite-control-set model predictive torque control with a deadbeat solution for PMSM drives," IEEE Trans. Ind. Electron., vol. 62, no. 9, pp. 5402–5410, Sep. 2015.

[22] J. Zhang, T. Sun, F. Wang, J. Rodríguez and R. Kennel, "A computationally efficient quasi-centralized DMPC for back-to-back converter pmsg wind turbine systems without dc-link tracking errors," IEEE Trans. Ind. Electron., vol. 63, no. 10, pp. 6160-6171, Oct. 2016.

[23] I. Jlassi and A. J. Marques Cardoso, "Fault-tolerant back-to-back converter for direct-drive PMSG wind turbines using direct torque and power control techniques," IEEE

Trans. Power Electron., vol. 34, no. 5, pp. 11215-1122, Nov. 2019.

[24] X. Wu, W. Song and C. Xue, "Low-complexity model predictive torque control method without weighting factor for five-phase PMSM based on hysteresis comparators," IEEE J. Emerg. Sel. Topics Power Electron., vol. 6, no. 4, pp. 1650–1661, Feb. 2018.

[25] I. Jlassi and A. J. Marques Cardoso, "Lookup-Table-Based Model Predictive Torque Control Without Weighting Factors for PMSM Drives," IECON 2019 - 45th Annual Conference of the IEEE Industrial Electronics Society, Lisbon, Portugal, 2019, pp. 1165-1170

[26] M. Habibullah, D. D. C. Lu, D. Xiao, and M. F. Rahman, "A simplified finite-state predictive direct torque control for induction motor drive," IEEE Trans. Ind. Electron., vol. 63, no. 6, pp. 3964–3975, Jun. 2016.

[27] I. Jlassi and A. J. Marques Cardoso, "Enhanced and computationally efficient model predictive flux and power control of PMSG drives for wind turbine applications," IEEE Trans. Ind. Electron., vol. 68, no. 8, pp. 6574-6583, Aug. 2021.

[28] M. Siami, D. Arab Khaburi and J. Rodriguez, "Simplified finite control set-model predictive control for matrix converter-fed PMSM drives," IEEE Trans. Power Electron., vol. 33, no. 3, pp. 2438-2446, Mar. 2018.

[29] M. Habibullah, D. D. C. Lu, D. Xiao, I. Osman, and M. F. Rahman, "Selected prediction vectors based FS-PTC for 3L-NPC inverter fed motor drives," IEEE Trans. Ind. Appl., vol. 53, no. 4, pp. 3588–3597,Jul./Aug. 2017.

[30] Y. Yang, H. Wen, M. Fan, M. Xie and R. Chen, "fast finite-switching-state model predictive control method without weighting factors for T-type three-level three-phase inverters," IEEE Trans. Ind. Inf., vol. 15, no. 3, pp. 1298-1310, Mar. 2019.

[31] T. Geyer and D. E. Quevedo, "Multistep finite control set model predictive control for power electronics," IEEE Trans. Power Electron., vol. 29, no. 12, pp. 6836–6846, Dec. 2014.

[32] Z. Zhang, C. Hackl, and R. Kennel, "Computationally efficient DMPC for three-level NPC back-to-back converters in wind turbine systems with PMSG," IEEE Trans. Power Electron., vol. 32, no. 10, pp. 8081–8034,Oct. 2017.

[33] A. V. Zakharov, S. I. Malafeev, and A. L. Dudulin, "Synchronous reluctance motor: Design and experimental research," in 2018 10th International Conference on Electrical Power Drive Systems, ICEPDS 2018 - Conference Proceedings, 2018.

[34] L. Xu and J. Yao, "A Compensated Vector Control Scheme of a Synchronous Reluctance

Motor Including Saturation and Iron Losses," IEEE Trans. Ind. Appl., vol. 28, no. 6, pp. 1330–1338, 1992.

[35] T. A. Lipo and D. W. Novotny, "Vector Control of a Synchronous Reluctance Motor Including Saturation and Iron Loss," IEEE Trans. Ind. Appl., vol. 27, no. 5, pp. 977–985, 1991.

[36] K. Yahia, D. Matos, J. O. Estima, and A. J. M. Cardoso, "Modeling synchronous reluctance motors including saturation, iron losses and mechanical losses," in 2014 International Symposium on Power Electronics, Electrical Drives, Automation and Motion, SPEEDAM 2014, 2014, pp. 601–606.

[37] I. Nasui-Zah, A. M. Nicorici, and C. Martis, "Saturation and cross-saturation in synchronous reluctance machines," in EPE 2018 - Proceedings of the 2018 10th International Conference and Expositions on Electrical And Power Engineering, 2018, pp. 347–351.

[38] Jung Ho Lee, Jung Chul Kim, and Dong Seek Hyun, "Effect analysis of magnet on Ld and Lq inductance of permanent magnet assisted synchronous reluctance motor using finite element method," IEEE Trans. Magn., vol. 35, no. 3, pp. 1199–1202, May 1999.

[39] H. A. Zarchi, G. R. A. Markadeh, and J. Soltani, "Direct Torque and Flux Regulation of Synchronous Reluctance Motor Drives Based on Input–Output Feedback Linearization", Energy Conversion and Management, vol. 51, no. 1, pp. 71- 80, 2010.

[40] Rashad, T. S. Radwan, M. A. Rahman, "A Maximum Torque per Ampere Vector Control Strategy for Synchronous Reluctance Motors Considering Saturation and Iron Losses", Conference Record of the 39th IAS Annual Meeting, vol. 4, p. 2411–2417, Oct 2004.

[41] H.-D. Lee, S.-J. Kang, and S.-K. Sul, "Efficiency-Optimized Direct Torque Control of Synchronous Reluctance Motor Using Feedback Linearization", IEEE Transactions on Industrial Electronics, vol. 46, no. 1, pp. 192-198, Feb 1999

[42] T. Lubin, H. Razik, and A. Rezzoug, "On-line efficiency optimization of a synchronous reluctance motor", Electric Power Systems Research, vol. 77, no. 5-6, pp. 484-493, 2007.

[43] R. Morales-Caporal and M. Pacas, "A Predictive Torque Control for the Synchronous Reluctance Machine Taking Into Account the Magnetic Cross Saturation," in IEEE Transactions on Industrial Electronics, vol. 54, no. 2, pp. 1161-1167, April 2007, doi: 10.1109/TIE.2007.891783.

[44] I. Jlassi and A. J. Marques Cardoso, "Model Predictive Current Control of Synchronous Reluctance Motors, Including Saturation and Iron Losses," 2018 XIII International Conference on Electrical Machines (ICEM), 2018, pp. 1598- 1603, doi:

10.1109/ICELMACH.2018.8506944.

[45] M. Hasegawa and H. Kitahara, "Extended-flux model with core-loss resistance of synchronous reluctance motors and torque estimation without core loss measurement and position encoder," Proceedings of the 2011 14th European Conference on Power Electronics and Applications, 2011, pp. 1-10.

[46] A. Vagati, M. Pastorelli, F. Scapino, and G. Franceschini, "Impact of cross saturation in synchronous reluctance motors of the transverse-laminated type," IEEE Trans. Ind. Appl., vol. 36, no. 4, pp. 1039–1046, Jul. 2000.

[47] R. G. Harley, D. J. N. Limebeer, and E. Chirricozzi, "Comparative study of saturation methods in synchronous machine models," IEE Proc. B Electr. Power Appl., vol. 127, no. 1, pp. 1–7, 1980.

[48] T. Lubin, H. Razik, and A. Rezzoug, "Magnetic Saturation Effects on the Control of a Synchronous Reluctance Machine," IEEE Power Engineering Review, vol. 22, no. 7. p. 51, 2002.

[49] A. M. El-Serafi, A. S. Abdallah, M. K. El-Sherbiny, and E. H. Badawy, "Experimental study of the saturation and the cross-magnetizing phenomenon in saturated synchronous machines," IEEE Trans. Energy Convers., vol. 3, no. 4, pp. 815–823, 1988.

[50] J. Bin Im, W. Kim, K. Kim, C. S. Jin, J. H. Choi, and J. Lee, "Inductance calculation method of synchronous reluctance motor including iron loss and cross magnetic saturation," in IEEE Transactions on Magnetics, 2009, vol. 45, no. 6, pp. 2803–2806.

[51] Hyeoun-Dong Lee, Seog-Joo Kang and Seung-Ki Sul, "Efficiency-optimized direct torque control of synchronous reluctance motor using feedback linearization," IEEE Trans. Ind. Electron., vol. 46, no. 1, pp. 192-198, Feb. 1999.

[52] D. Matos, J. Estima, Y. Khaled and A. J. Marques Cardoso, "Modeling and implementation of MTPA control strategy for synrm variable speed drives," Int. Jour. Elec. Eng.. 9. 1103. 10.15866/iree.v9i6.4357. 2014.

[53] H. Hadla and S. Cruz, "Predictive Stator Flux and Load Angle Control of Synchronous Reluctance Motor Drives Operating in a Wide Speed Range," in IEEE Transactions on Industrial Electronics, vol. 64, no. 9, pp. 6950-6959, Sept. 2017, doi: 10.1109/TIE.2017.2688971.

[54] P. Cortes, J. Rodriguez, C. Silva, and A. Flores, "Delay compensation in model predictive current control of a three-phase inverter," IEEE Trans. Ind. Electron., vol. 59, no. 2, pp. 1323–1325, Feb. 2012.

[55] J. Rodriguez et al., "Predictive Current Control of a Voltage Source Inverter," in IEEE Transactions on Industrial Electronics, vol. 54, no. 1, pp. 495-503, Feb. 2007, doi: 10.1109/TIE.2006.888802.

[56] dSPACE FAQ 23, Measuring Execution Times of Block and Subsystems, 4 pp., dSPACE GmbH, Paderborne, Germany, 2011.

[57] "IEEE Recommended Practices and Requirements for Harmonic Control in Electrical Power Systems," in IEEE Std 519-1992, vol., no., pp.1-112, 9 April 1993, doi: 10.1109/IEEESTD.1993.114370.

Appendix A

Computational Simulation Settings

A.1. Simulation Schematics of the SynRM Drive

The main SynRM Drive Simulation Schematics used for the implementation of the proposed control strategy in the Matlab/Simulink software are presented in this section.

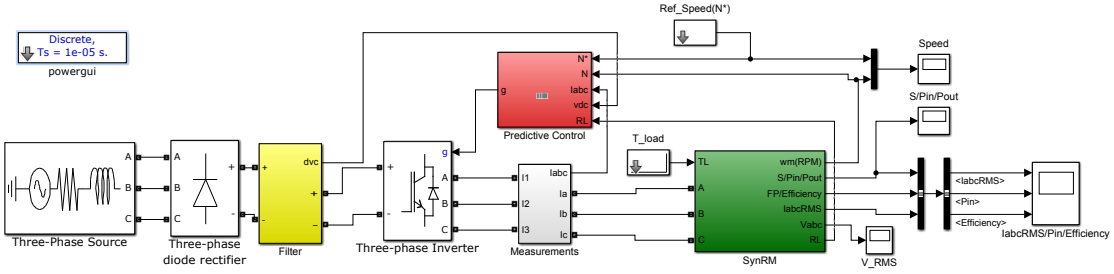

Figure A.1: General schematics of the SynRM drive implemented in Matlab/Simulink.

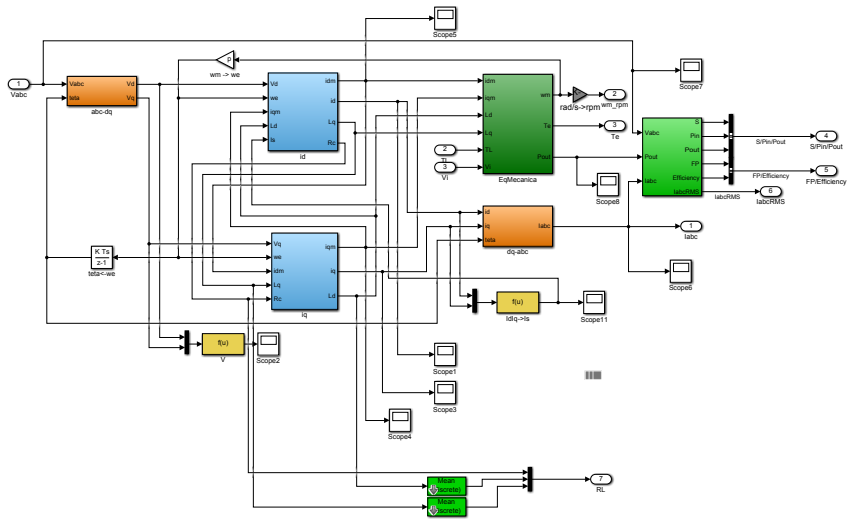

Figure A.2: General schematic of the SynRM dynamic model implemented in Matlab/Simulink.

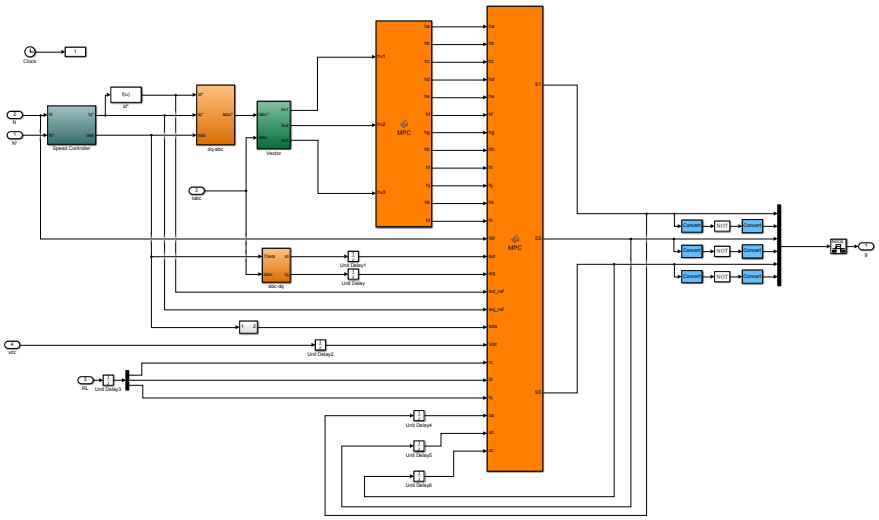

Figure A.3: General schematic of the proposed HCC-MPCC strategy implemented in Matlab/Simulink.

A.2. Simulation Drive Settings

The pre-defined parameters of the main drive components of the SynRM Drive Simulation Schematics used to implement the proposed control strategy in the Matlab/Simulink software are presented in this section.

Table A.1: Parameters of the three-phase grid supply block

Phase-to-phase rms voltage	410 V
Phase angle of phase A	0º
Frequency	50 Hz
Internal Connection	Yg
Source Resistance	0.5 Ω
Source Inductance	1 µH

Table A.2: Parameters of the three-phase diode bridge rectifier block

Snubber Resistance	100 kΩ
Snubber Capacitance A	20 nF
R_{on}	0.01Ω
L_{on}	0 H
Forward Voltage	0.7 V

Table A.3: Parameters of the DC bus capacitor filter block

Capacitance	2350 µF
Initial Voltage A	150 V

Table A.4: Parameters of the three-phase inverter block

Snubber Resistance	3500 kΩ
Snubber Capacitance A	inf
R_{on}	11.5 mΩ
Forward Voltages	1.2 V, 1.3 V
Tf(s), Tt(s)	1 µs, 2 µs

Table A.5: Complementary parameters of the SynRM dynamic model

R_s	1.71 Ω
J	0.0137 kg.s2
B_m	0.00036 Nms/rad
p	2
L_d	0.24 H
L_q	0.057 H

A.3. Predictive Control Settings

The pre-defined parameters of the predictive control block used throughout to implement the proposed control strategy in the Matlab/Simulink software are presented in this section.

Table A.6: PI Gains and HCC bandwidth

K_p	0.08
K_i	0.8
bh	0.2 A